Co–Fe–Cr (oxy)Hydroxides as Efficient Oxygen Evolution Reaction Catalysts

Junsheng Chen, Hao Li, Shuangming Chen, Jingyuan Fei, Chang Liu, Zixun Yu, Kihyun Shin, Zongwen Liu, Li Song, Graeme Henkelman, Li Wei,* and Yuan Chen*

Transition metal cobalt (oxy)hydroxides are promising catalyst candidates for the oxygen evolution reaction (OER). Their activity can be significantly enhanced by doping chromium; however, the optimal catalyst elemental composition is unknown, and the exact role of Cr remains elusive. Here, density functional theory (DFT) calculations and comprehensive catalyst characterization are combined to address these two questions. Guided by DFT calculations, a series of amorphous ternary Co-iron(Fe)-Cr (oxy)hydroxides with systematically tuned elemental compositions are synthesized. Performance atlases of these catalysts are established based on different experimental descriptors, which show that the optimal $Co_5Fe_3Cr_2$ (oxy)hydroxide reaches a current density of 10 mA cm^{-2} at an overpotential of 232 mV. It delivers a Co-based mass activity of 1486 A g^{-1} and a high turnover frequency of 0.23 s^{-1}, over two orders higher than monometallic Co (oxy)hydroxide. X-ray absorption and photoelectron spectroscopies reveal that Cr promotes Co atoms to occupy octahedral sites and modifies the Co electronic structure. Quasi-operando electron energy loss spectroscopy further experimentally confirm that Cr accelerates the pre-oxidation of Co^{2+} to higher valence species, resulting in significantly higher catalytic activity. The findings here pave the way to use Co–Fe–Cr (oxy)hydroxides as an efficient OER catalyst.

1. Introduction

Oxygen evolution reaction (OER) is a critical limiting factor in various energy conversion and storage devices, including water

J. Chen, J. Fei, C. Liu, Z. Yu, Z. Liu, L. Wei, Y. Chen
School of Chemical and Biomolecular Engineering
The University of Sydney
Darlington, NSW 2008, Australia
E-mail: l.wei@sydney.edu.au; yuan.chen@sydney.edu.au
H. Li,[+] K. Shin, G. Henkelman
Department of Chemistry and the Oden Institute
for Computational and Engineering Sciences
The University of Texas at Austin
105 E. 24th Street, Stop A5300, Austin, TX 78712, USA
S. Chen, L. Song
National Synchrotron Radiation Laboratory
CAS Center for Excellence in Nanoscience
University of Science and Technology of China
Hefei, Anhui 230029, P. R. China

(iD) The ORCID identification number(s) for the author(s) of this article can be found under https://doi.org/10.1002/aenm.202003412.

[+]Present address: Catalysis Theory Center, Department of Physics, Technical University of Denmark, 2800 Lyngby, Denmark

DOI: 10.1002/aenm.202003412

electrolyzers and rechargeable metal-air batteries.[1] This complex four-electron reaction involves multiple reaction intermediates and in situ catalyst structural changes, requiring considerable energy input. Ir and Ru oxides show relatively high catalytic activity for OER; however, their high cost and poor stability severely limit their applications. Recent studies show that some first-row earth-abundant transition metal (oxy)hydroxides are promising catalyst candidates for OER.[2] Among them, cobalt (Co) (oxy)hydroxides have drawn intensive interest because Co in (oxy)hydroxides exhibits an intermediate $t_{2g}^5 e_g^1$ electron configuration which interacts with O intermediates (e.g., OH*, O*, and OOH*) favorably for the OER.[3]

Co species undergo redox transitions, that is, Co^{2+}/Co^{3+} and Co^{3+}/Co^{4+}, during OER and the high valence Co species ($Co^{3+\delta}$, $1 > \delta > 0$) have been recognized as active catalytic centers.[4] This process requires significant transformation energy. Lowering this transformation energy may improve the catalytic activity. For example, W^{6+} with entirely vacant d-orbitals can accept electrons from Co and promote the transformation from Co^{2+} to Co^{3+} in a ternary Co-Fe-W catalyst, resulting in one of the best OER catalysts reported recently.[4d] The similar effect by Mo has been demonstrated as well.[5] Further, experimental and computational studies suggest that modifying Co sites′ local environment can optimize their interactions with O intermediates and improve catalytic activity.[6] Several approaches have been explored, such as creating O or metal vacancies,[7] substituting O with B, N, P, or S,[8] or doping other transition metals, such as Fe, Mn, and Ni.[9] Chromium (Cr) is in the same group as W on the periodic table. Cr^{6+} may also promote the catalytic activity of Co. The abundance of Cr is 127 times more than W in the earth's crust, and it is much cheaper than W; thus, it may enable more cost-effective Co (oxy)hydroxide catalysts. Although several studies have explored using Cr to promote the OER activity of Co,[10] the exact role of Cr played has not been fully understood, and the optimal catalytic elemental composition is still unknown.

Here, we first used density functional theory (DFT) calculations to predict the Co site's structural transformation energy requirements in ternary Co–Fe–Cr (oxy)hydroxides. The site-specific catalytic activity for OER was estimated based on the

well-established OER activity volcano plot. Guided by theoretical predictions, we synthesized a series of Co–Fe–Cr (oxy)hydroxides (denoted as $Co_aFe_bCr_c$, $a + b + c = 10$) using a co-precipitation method at a low synthesis temperature without high-temperature pyrolysis. Their structural and electronic properties were characterized systematically by X-ray absorption and photoelectron spectroscopy (XAS and XPS) and electron energy loss spectroscopy (EELS) to understand the critical role of Cr. The optimal elemental composition was identified, which delivered an excellent catalytic performance for OER in both alkaline and neutral electrolytes together with high stability, outperforming noble metal based IrO_2 catalysts.

2. Results and Discussion

Recent studies proposed that a catalytically active Co^{2+} or Co^{3+} site in Co (oxy)hydroxides would undergo sequential proton-coupled electrochemical steps to form the high valence Co^{4+}, which accepts electrons from adsorbed reaction intermediates to complete an OER cycle.[4a,b,11] The Co site valence state evolution and subsequent structural transformations are critical for their catalytic activities. We first calculated the free energy (ΔG) of $Co^{2+} \rightarrow Co^{3+} \rightarrow Co^{4+}$ transitions in bulk Co-based mono, binary, and ternary metal (oxy)hydroxides. The computational and modeling details are described in the Supporting Information. **Figure 1**a shows that the formation energies of Co^{3+} and Co^{4+} decrease when Co is partly replaced by Fe or Cr, indicating that lower anodic potentials are required to form these high valence Co sites in binary metal (oxy)hydroxides. The significantly lower $\Delta G(Co^{2+} \rightarrow Co^{3+})$ on CoCrOOH suggests that Cr can promote the formation of Co^{3+}. The lowest $\Delta G(Co^{3+} \rightarrow Co^{4+})$ is on CoFeOOH, indicating that Fe can stabilize Co^{4+}. These

strong synergies among Cr, Fe, and Co in CoFeCrOOH result in $\Delta G(Co^{2+} \rightarrow Co^{3+})$ and $\Delta G(Co^{3+} \rightarrow Co^{4+})$ between that of CoCrOOH and CoFeOOH, which may promote the structural transformation toward high valence Co sites.

To further predict the surface reactivity of Co–Fe–Cr (oxy)hydroxides, we used an OER volcano activity plot to analyze the activity trends based on a β-CoOOH (10$\bar{1}$4) surface, which is regarded the most thermodynamically favorable Co hydroxide surface under OER potentials.[6a,12] Using the models displayed in Figure 1c, the volcano plot in Figures 1b shows that doping Fe and Cr into β-CoOOH can create surface sites with higher OER activity. Meanwhile, highly active dopant sites (e.g., the Fe or Cr sites) can form directly. The calculated projected density of states (PDOS) of these surfaces is shown in Figure S1, Supporting Information. The ternary Co–Fe–Cr surface has the highest d-electron density near the Fermi level (E_f, –0.5–0.5 eV), which is mainly due to Co d-electrons, suggesting that Co is the primary catalytically active site in these models.[13] These DFT calculations suggest that ternary Co–Fe–Cr (oxy)hydroxides with a suitable metal elemental composition may serve as high-performance OER catalysts with a high density of active Co sites with improved site-specific activity.

Guided by the above theoretical predictions, we used a straightforward co-precipitation method to synthesize a series of ternary $Co_aFe_bCr_c$ (oxy)hydroxides to discover the optimum elemental composition. As described in detail in Supporting Information, $CoCl_2 \cdot 6H_2O$, $FeCl_3 \cdot 6H_2O$, and $KCr(SO_4)_2 \cdot 12H_2O$ aqueous solutions were mixed at different molar ratios, keeping the total metal anion concentration at 20 mм. The precursor solution was then injected into a urea solution (50 mL, 0.2 м) in 20 min under vigorous stirring and followed by stirring at 90 °C for 6 h. Precipitated $Co_aFe_bCr_c$ (oxy)hydroxides were collected by centrifugation, washed with deionized (DI) water
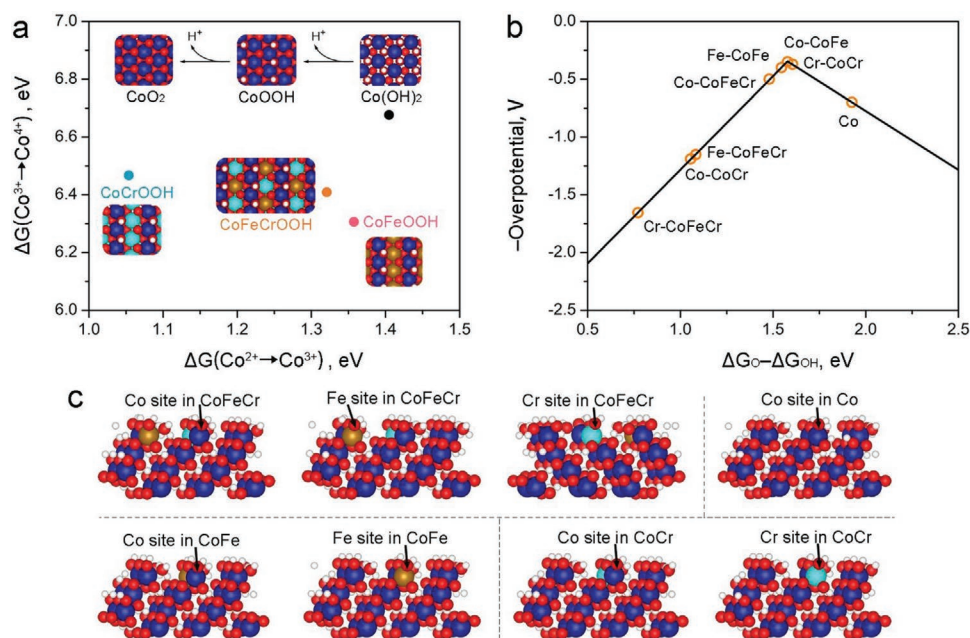

Figure 1. Theoretical prediction. a) Free energies of $Co^{2+} \rightarrow Co^{3+} \rightarrow Co^{4+}$ evolution in various Co–Fe–Cr (oxy)hydroxides. b) Theoretical OER volcano plot. c) Optimized β-CoOOH (10$\bar{1}$4) models considered for DFT calculations. Red, white, blue, brown, and teal spheres represent O, H, Co, Fe, and Cr atoms, respectively.
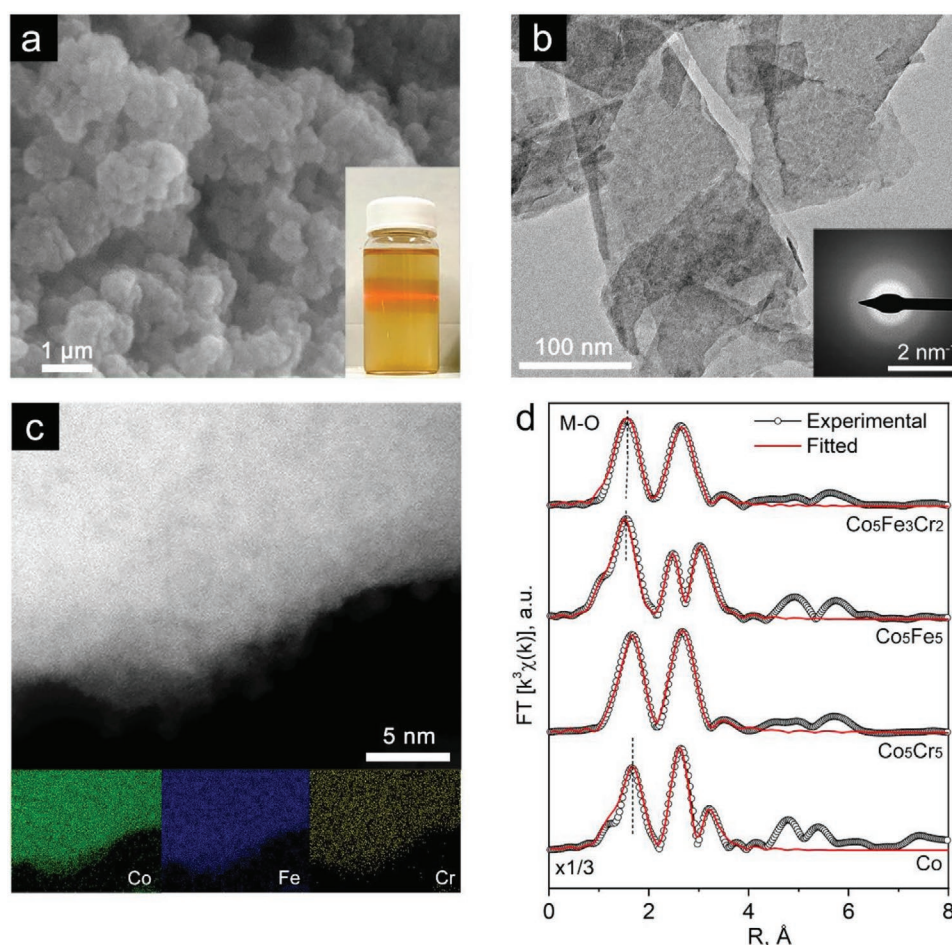
**ADVANCED
SCIENCE NEWS**

www.advancedsciencenews.com

**ADVANCED
ENERGY
MATERIALS**

www.advenergymat.de

Figure 2. Atomic structure analysis of $Co_aFe_bCr_c$ (oxy)hydroxides. a) SEM and b) TEM images of $Co_5Fe_3Cr_2$ (oxy)hydroxide. The inset in (a) shows a stable colloid water solution of $Co_5Fe_3Cr_2$. The inset of (b) shows the corresponding SAED pattern. c) A HAADF-STEM image and the related EDX elemental mapping results. d) The k^3 weighted-FT EXAFS spectra of Co K-edge in different catalysts.

and ethanol, and finally dried at 60 °C. The scanning electron microscope (SEM) image in **Figure 2**a shows that a representative catalyst ($Co_5Fe_3Cr_2$ (oxy)hydroxides) comprises aggregated microspheres with a diameter of around 1 µm. Other binary (e.g., Co_5Fe_5 and Co_5Cr_5 (oxy)hydroxides) and unitary (Co (oxy)hydroxides) catalysts show similar morphological structures (Figure S2, Supporting Information). The microspheres can be dispersed in water by mild bath sonication, forming a stable colloid suspension with typical Tyndall scattering lines (inset of Figure 2a). The energy-dispersive X-ray spectroscopy (EDX) elemental compositions displayed in Figure S2, Supporting Information suggest a Co:Fe:Cr atomic ratio of 4.95:3.03:2.02 in $Co_5Fe_3Cr_2$ (oxy)hydroxides close to the designed target. Table S1, Supporting Information shows that the atomic ratios determined by EDX are similar to the results obtained by XPS and the bulk analysis by inductively-coupled plasma atomic emission spectroscopy (ICP-AES). The oxygen contents are also determined from ICP-AES measurement, and the results are listed in Table S1, Supporting Information. The transmission electron microscope (TEM) image in Figure 2b shows that $Co_5Fe_3Cr_2$ (oxy)hydroxides comprise crumpled nanosheets without observable lattice fringes. They have low crystallinity,

supported by diffusive rings in the selected area electron diffraction pattern (SAED, inset of Figure 2b) and weak X-ray diffraction pattern (XRD, Figure S3, Supporting Information). Although weak features belong to CoFe layered double hydroxides can be identified, the multimetal samples display a gradual deterioration in the crystallinity, suggesting that incorporating Fe and/or Cr heavily distort the crystal lattice. A high-angle annular dark-field scanning TEM image (HAADF-STEM, Figure 2c) shows no prominent contrast spots of metal particles. The corresponding EDX elemental mappings further confirm a homogeneous elemental distribution in $Co_5Fe_3Cr_2$ (oxy)hydroxides.

The atomic arrangement of the different metal elements in $Co_5Fe_3Cr_2$ (oxy)hydroxides was investigated by extended X-ray absorption fine structure (EXAFS) analysis at their K-edges. Figure 2d and Figure S4–S6, Supporting Information show a prominent single metal (M)-O peak in the first shell of their k^3-weighted Fourier-transformed ($k^3\chi(k)$-FT) EXAFS spectra. The first-shell M—O bond lengths and the coordination number were fitted, and the results are summarized in Table S2, Supporting Information. Figure 2d shows that Fe and Cr incorporation have different effects on the Co—O bond length.

Monometallic Co (oxy)hydroxides have a bond length of 1.973 Å. Fe doping contracts the Co—O bond length to 1.924 Å in Co_5Fe_5 (oxy)hydroxides, while Cr has a less impact with a similar length of 1.978 Å in Co_5Cr_5 (oxy)hydroxides. Partial replacement of Fe with Cr leads to a slightly expanded Co—O length to 1.938 Å in $Co_5Fe_3Cr_2$ (oxy)hydroxides. The first shell Fe—O and Cr—O bond length also show slight expansion in $Co_5Fe_3Cr_2$ (oxy)hydroxides. These bond length changes suggest strong interactions among Co, Fe, and Cr can alter their atomic arrangements in $Co_aFe_bCr_c$ (oxy)hydroxides. Figure 2d also shows that the second-shell Co-Co features of Co_5Fe_5 and Co (oxy)hydroxides split into two peaks, suggesting the co-existence of Co centers in octahedral (Co_{Oh}) and tetrahedral (Co_{Td}) coordinations. This agrees well with their fitted coordination numbers at 5.2 ± 1.2 and 5.1 ± 0.3, respectively. $Co_5Fe_3Cr_2$ and Co_5Cr_5 (oxy)hydroxides have larger Co coordination numbers at 5.8 ± 0.4 and 5.7 ± 0.6, indicating that the incorporation of Cr promotes Co atoms to occupy octahedral sites.[14] Further, Figure S5 and Table S2, Supporting Information show that Fe mainly occupies octahedral sites (Fe_{Oh}). The coordination number of Cr exhibits a substantial drop from 5.6 ± 0.4 in Co_5Cr_5 (Cr_{Oh} dominating) to 4.4 ± 0.6 in ternary $Co_5Fe_3Cr_2$ (oxy)hydroxides, suggesting the formation of abundant Cr in the fourfold coordination.[4b]

The electronic structures of Co, Fe, and Cr in $Co_aFe_bCr_c$ (oxy)hydroxides were assessed by XPS, EELS, and X-ray absorption near-edge structure (XANES). **Figure 3**a displays high-resolution Co2p XPS spectra, which split into $Co2p_{3/2}$ and $Co2p_{1/2}$ orbitals. The deconvolution results indicate the co-existence of Co^{3+} (780.6 and 796.4 eV) and Co^{2+} (782.3 and 798.1 eV). Incorporating Fe resulted in an increased abundance of Co^{3+} in $Co_5Fe_3Cr_2$ (31.1 at%) and Co_5Fe_5 (40.8 at%) (oxy)hydroxides in comparison to 9.3 at% in monometallic Co (oxy)hydroxides. On the contrary, incorporating Cr exhibited a negligible effect with a Co^{3+} abundance of 11.3 at% in Co_5Cr_5 (oxy)hydroxides. When Cr partially replaces Fe in $Co_5Fe_3Cr_2$ (oxy)hydroxides, the Co^{3+} abundance reduces slightly. The Co2p

XPS spectra of a series $Co_5Fe_bCr_{5-b}$ (oxy)hydroxides ($b = 0–5$, Figure S7, Supporting Information) shows that the abundance of Co^{3+} and Fe/Co ratio has a monotonic relationship. The strong electronic interactions among these metals also alter the electronic structures of Fe and Cr. Figure S8, Supporting Information displays that Fe $2p_{3/2}$ peaks in the $Co_5Fe_3Cr_2$ and Co_5Fe_5 (oxy)hydroxides are broadened and red-shifted about 0.3 and 0.6 eV, respectively, compared to Fe (oxy)hydroxide, indicating reduced Fe valence states. $Cr2p_{3/2}$ peaks in Cr and Co_5Cr_5 (oxy)hydroxides are similar to that of Cr^{3+}. In contrast, trimetallic $Co_5Fe_3Cr_2$ (oxy)hydroxides contain abundant Cr^{2+} (52 at%, Figure S9, Supporting Information). Cr^{2+} was reported to situate in fourfold coordination (tetrahedral or square-planar) preferentially,[15] which may promote the Co occupation in octahedral sites in $Co_5Fe_3Cr_2$ (oxy)hydroxides, agreeing with our EXAFS fitting results.

We further collected the EELS spectra of Co, Fe, Cr, and O in $Co_aFe_bCr_c$ (oxy)hydroxides. The spectra were normalized following an established method (see details and Figure S10, Supporting Information).[16] Figure 3b shows that the Co-L_3 edges of $Co_5Fe_3Cr_2$ and Co_5Fe_5 (oxy)hydroxides blue-shift by about 1.35 eV with increased white-line intensities compared with Co and Co_5Cr_5 (oxy)hydroxides, indicating higher Co valence states. Their Co L_3/L_2 edge ratios, a sensitive Co valence descriptor, are also higher (inset in Figure 3b).[17] The partial replacement of Fe with Cr changed the 3d-orbital occupancy of both metals in $Co_5Fe_3Cr_2$ (oxy)hydroxides. The preferential electron extraction from Fe by Cr resulted in an increased Fe-L_3 edge white-line intensity in $Co_5Fe_3Cr_2$ (oxy)hydroxides (Figure 3c). Inversely, the higher Cr d-orbital filling density reduced the Cr L_3-edge intensity (Figure 3d), consistent with surface-sensitive XPS results (Figure S9, Supporting Information).[16b] Following a previously reported method, we further calculated the peak area ratio (I_w) between the Co—L edge after baseline removal ($I_w = L_3/(L_2 + L_3)$) to gain insights on the Co spin-state.[18] Simulated EELS spectra afford I_w values of 0.83, 0.66, and 0.77 for Co_{Oh}^{2+} in

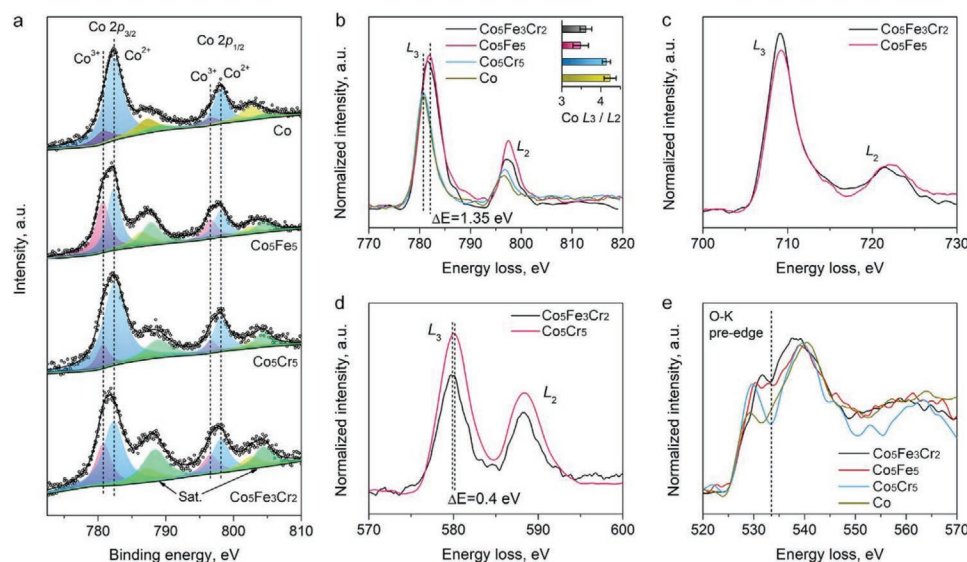**Figure 3.** Electronic structures of $Co_aFe_bCr_c$ (oxy)hydroxides by spectroscopies. a) XPS spectra and EELS spectra of b) Co, c) Fe, d) Cr, and e) O in various catalysts. Inset of (b): Calculated Co L_3/L_2 intensity ratios in $Co_aFe_bCr_c$ (oxy)hydroxides.

**ADVANCED
SCIENCE NEWS**

www.advancedsciencenews.com

**ADVANCED
ENERGY
MATERIALS**

www.advenergymat.de

high-spin (Co_{Oh}^{2+}-HS), and Co_{Oh}^{3+} in both low-spin and high-spin (Co_{Oh}^{3+}-LS and -HS), respectively (Figure S11, Supporting Information). The identical values of 0.809 and 0.805 for Co and Co_5Cr_5 (oxy)hydroxides suggest both samples are enriched with Co_{Oh}^{2+}-HS. The electronic interaction between Fe^{3+} and Co^{2+} results in the formation of abundant Co_{Oh}^{3+}-LS, affording a decreased I_w of 0.751 for Co_5Fe_5 (oxy)hydroxides. While Cr is further introduced, the increased I_w value of 0.792 for the trimetallic $Co_5Fe_3Cr_2$ (oxy)hydroxides indicates the Co spin state's further fine-tuning with the formation of Co_{Oh}^{3+}-HS. Such spin-transition of Co_{Oh}^{3+} between high-spin and low spin may eventually lead to the optimal structure (e.g., $t_{2g}^5 e_g^1$), for the OER intermediate adsorption.[3]

We further examined the O K-edge EELS spectra. The pre-edge originated from the O1s contribution to unoccupied metal 3d–O2p bands in different samples exhibit varied intensity.[19] The higher intensity of the O K-edge pre-edge peak is indicative of M–O bonds with higher electron density, which can improve the M–O bond covalency, leading to higher OER activity.[20] Figure 3e shows that the pre-edge intensity has a clear trend as $Co_5Fe_3Cr_2$ (oxy)hydroxides > Co_5Fe_5 (oxy)hydroxides ≈ Co_5Cr_5 (oxy)hydroxides > Co (oxy)hydroxides, suggesting high OER activity in $Co_5Fe_3Cr_2$ (oxy)hydroxides. These spectroscopic results also agree with our calculated O PDOS near the Fermi level (Figure S12, Supporting Information). Further, the above XPS and EELS results agree with Co, Fe, and Cr K-edge XANES results (Figure S13, Supporting Information). Overall, our comprehensive electronic analysis suggests that the incorporation of Cr can modify electronic structures of Co–Fe–Cr (oxy)hydroxides and enhance their OER activity.

The $Co_aFe_bCr_c$ (oxy)hydroxides and reference catalysts' catalytic performances for OER were assessed in O_2 saturated 1 M KOH. Each catalyst was deposited on glassy-carbon rotating disk electrodes (GCEs) at the same mass loading of 0.2 mg cm^{-2}. We created ternary performance atlases (**Figure 4**a–c) of $Co_aFe_bCr_c$ (oxy)hydroxides based on three catalytic performance descriptors: 1) The overpotential required to reach a geometric current density (j) of 10 mA cm^{-2} (η_{10}), 2) the Tafel slope, and 3) the turnover frequency (TOF) at η of 300 mV based on the total metal moles in the catalysts.

Figure 4d displays linear sweep voltammetry (LSV) curves of representative $Co_aFe_bCr_c$ (oxy)hydroxides and commercial IrO_2. The optimal elemental composition to achieve the best catalytic performance based on Figure 4a is Co:Fe:Cr = 5:3:2 ($Co_5Fe_3Cr_2$ (oxy)hydroxides), which exhibits the smallest η_{10} of 232 mV. This value is comparable or even better than some recently reported Cr containing trimetallic catalysts.[10d–g] In comparison, η_{10} of Co_5Fe_5, Co_5Cr_5, and Co (oxy)hydroxides and IrO_2 is 276, 305, 392, and 316 mV, respectively (see detailed comparisons in Table S3, Supporting Information). Under the η of 300 mV, $Co_5Fe_3Cr_2$ (oxy)hydroxides deliver a mass activity of 477.0 A g^{-1} (based on the total mass of the catalyst), which is about 2.8, 11.2, and 60.4 times higher than that of bimetallic Co_5Fe_5, Co_5Cr_5, and unitary Co (oxy)hydroxides, respectively. The activity of $Co_5Fe_3Cr_2$ (oxy)hydroxides based on the mass of Co can reach 1486.0 A g^{-1}, which is over 120 times higher than that of Co (oxy)hydroxides. We further compared their catalytic performance normalized by their electrochemical active surface area (ECSA) determined by the cyclic voltammetry (CV, see details in

Experimental Section and Figure S14, Supporting Information) scans. Figure S15, Supporting Information shows their areal specific capacitance and LSV curves normalized by their ECSA. We plotted the overpotential ($\eta_{ECSA-0.1}$) required to deliver an ECSA normalized current density (j_{ECSA}) of 0.1 mA cm^{-2} in Figure S16, Supporting Information, and the performance is similar to Figure 4a, which is based on η_{10} values.

Figure 4e shows Tafel plots of catalysts, which describe their reaction kinetics. $Co_5Fe_3Cr_2$ (oxy)hydroxides have the smallest Tafel slope of 31 mV dec^{-1}. $Co_5Fe_3Cr_2$ (oxy)hydroxides also display the highest TOF of 0.12 s^{-1} based on Figure 4c, which is nearly two orders of magnitude higher than the monometallic Co (oxy)hydroxides at 0.0017 s^{-1}. If we calculated TOF based on Co alone in the catalysts, $Co_5Fe_3Cr_2$ (oxy)hydroxides have a TOF of 0.23 s^{-1} (Table S3, Supporting Information). Nyquist plots obtained by electrochemical impedance spectroscopy (EIS) show that $Co_5Fe_3Cr_2$ (oxy)hydroxides have the smallest charge transfer resistance (R_{CT}) of 5.4 ohms (Figure S17 and Table S4, Supporting Information). It also exhibits the smallest oxide resistance (R_O) of 3.2 ohms. Mott–Schottky plots in Figure S18 and Table S4, Supporting Information shows that $Co_5Fe_3Cr_2$ (oxy)hydroxides also have the highest near-surface carrier density of 6.2×10^{19} cm^{-2}. We also found that the amorphous crystal structure of $Co_5Fe_3Cr_2$ (oxy)hydroxides is essential for its excellent OER activity. We thermally annealed $Co_5Fe_3Cr_2$ (oxy)hydroxides at 500 °C (denoted as A-$Co_5Fe_3Cr_2$). A-$Co_5Fe_3Cr_2$ contains segregated crystalline phases, as indicated by XRD and TEM results (Figure S19, Supporting Information). This catalyst exhibits inferior catalytic performance with a significantly increased η_{10} at 373 mV, higher R_{CT} of 19.96 ohms, and a much lower near-surface carrier density of 1.2×10^{19} cm^{-2}. Overall, $Co_5Fe_3Cr_2$ (oxy)hydroxides deliver one of the best catalytic activity among recently reported CoFe-based OER catalysts. The detailed comparison is listed in Table S5, Supporting Information.

The stability of $Co_5Fe_3Cr_2$ (oxy)hydroxides was assessed by continuous discharging at 50 mA cm^{-2} in 1 M KOH electrolyte (Figure 4f). The catalyst was loaded on a gold rotary disk electrode at 0.2 mg cm^{-2}. A Ni_4Mo catalyst loaded on a Ni foam (Ni_4Mo/NF, Figure S20, Supporting Information) was prepared as the counter electrode.[21] After a 168 h test, the overpotential increased marginally by 36 mV. TEM analysis confirmed the poor crystallinity of $Co_5Fe_3Cr_2$ (oxy)hydroxides (Figure S21, Supporting Information). Metal leaching monitored by periodical ICP-AES measurement suggests that there are negligible Co and Fe leaching, and the constant Co/Fe ratio is well-maintained (Figure 4f). About 7% of Cr leached during the first 12 h, and the remaining Cr is stable. Post-test XPS spectra of Co, Fe, and Cr show a red-shifted Co 2p$_{3/2}$ peak ($\Delta E = 0.9$ eV) and a blue-shifted Fe 2p$_{3/2}$ ($\Delta E = 0.1$ eV), indicative of increased Co^{3+} and Fe^{3+} abundances (Figure S22, Supporting Information). The Cr2p XPS spectrum exhibits a substantial change with the diminish of Cr^{2+} and the formation of abundant Cr^{6+} (≈82 at%). The higher valence Cr species are expected to facilitate electron removal from Co and stabilize high valent Co.[4d]

We further calculated the detailed reaction free energies at various metal sites using the models shown in Figure 1c, which could provide more accurate insights compared to the volcano-based prediction (Figure 1b). The following four OER reaction
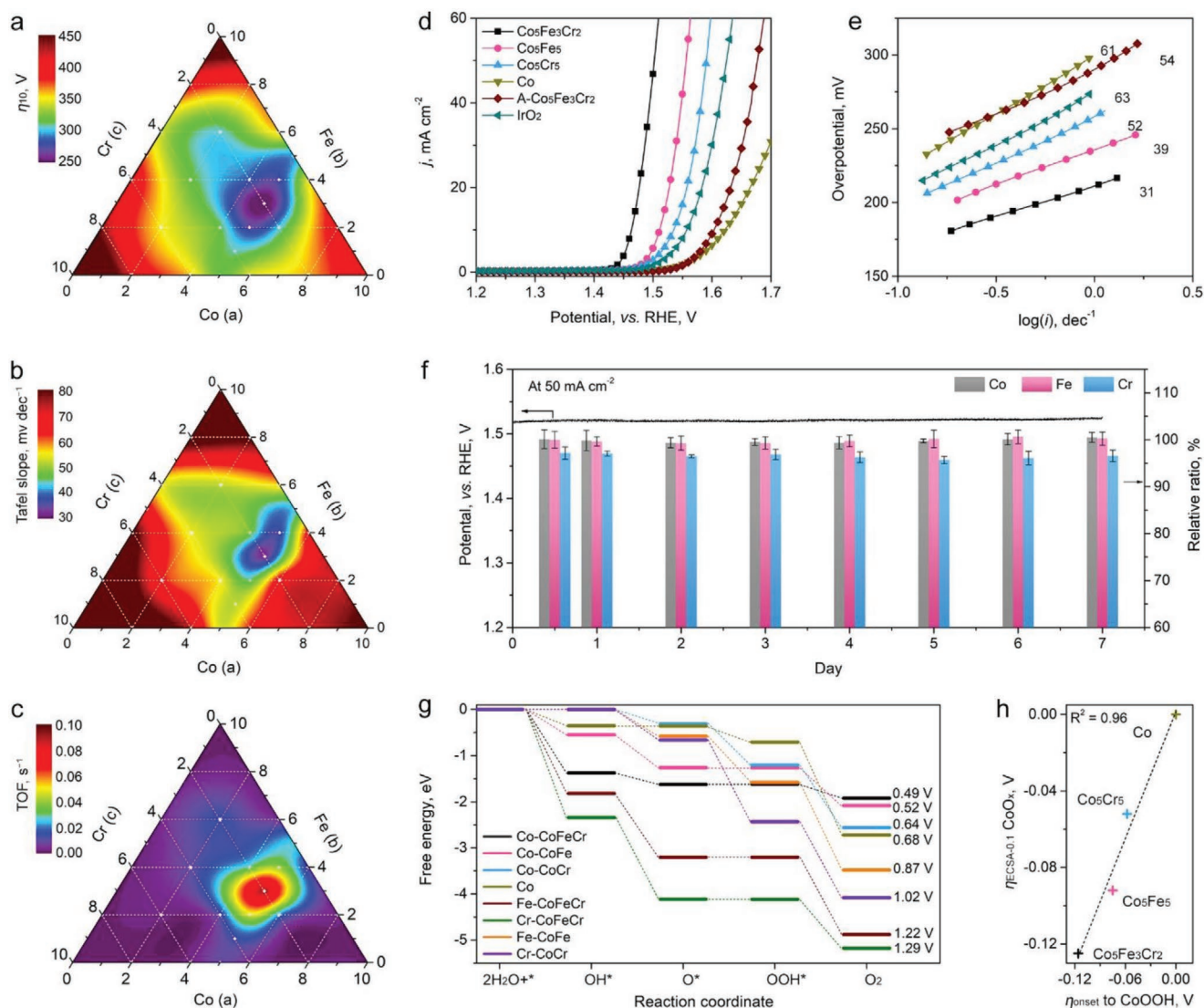
Figure 4. OER catalytic performance atlases of $Co_aFe_bCr_c$ (oxy)hydroxides measured in 1 M KOH electrolyte based on a) η_{10}, b) Tafel slope, and c) TOF at the η of 300 mV. d) LSV curves (with 95% iR-compensation) and e) Tafel plots of representative $Co_aFe_bCr_c$ (oxy)hydroxides and references. f) Chronopotentiometric stability tests of $Co_5Fe_3Cr_2$ (oxy)hydroxides (without iR-compensation) and ICP-AES metal element retention. g) Calculated free energy diagrams of different surface models described in Figure 1c. h) Correlation between the theoretical and experimental overpotentials. The values are referenced to the CoOOH model and the monometallic Co sample, respectively.

steps (* denotes a surface site) involving different reaction intermediates were used in our calculations (see computational details in Supporting Information).[6a]

$$H_2O + * \rightarrow *OH + H^+ + e^- \quad (1)$$

$$*OH \rightarrow *O + H^+ + e^- \quad (2)$$

$$H_2O + *O \rightarrow *OOH + H^+ + e^- \quad (3)$$

$$*OOH \rightarrow O_2 + H^+ + e^- + * \quad (4)$$

Previous studies have shown that this mechanism leads to good agreement between theoretical and experimental overpotentials in both alkaline and acidic conditions for many metal oxides.[6a,12] The theoretical overpotential (η_{theo}) was determined

as $\eta_{theo} = Max[G_1, G_2, G_3, G_4]/e - 1.23$ V, where G_1–G_4 represent the free energies of the four elementary steps (Table S6, Supporting Information).[22] Figure 4g compares free-energy diagrams at the various active sites at their η_{theo}. With both Fe and Cr, the lowest η_{theo} of 0.49 V was found at Co sites in the ternary CoFeCr model. Figure 4h reveals an excellent qualitative agreement between our theoretical calculations and experiments: The η_{theo} shows a nearly linear relationship with the experimentally measured onset overpotential ($j_{ECSA-0.1}$) by using monometallic CoOOH as a theoretical reference and monometallic Co sample as the experimental reference, further confirming that incorporating Fe and Cr can significantly improve the catalytic activity of Co.

Our DFT calculations suggest that the incorporation of Fe and Cr promotes the deprotonation-coupled pre-oxidation of

Co^{2+} to OER active higher valence species (Co^{3+} or $Co^{3+\delta}$).[4b,9b,11] To validate our theoretical results, we first compared the ECSA normalized 1st and 2nd CV curves of various samples. Figure S23, Supporting Information shows that all the catalysts have two prominent oxidation peaks at $\approx$1.1 V (Peak I, Co^{2+} to Co^{3+}) and 1.4 V (Peak II, Co^{3+} to Co^{4+}).[23] Peak I in Cr doped $Co_5Fe_3Cr_2$ and Co_5Cr_5 shifts cathodically by $\approx$30 mV compared to Co (oxy) hydroxide, indicating accelerated Co^{2+} oxidation. The change in Peak II in Fe doped $Co_5Fe_3Cr_2$ and Co_5Fe_5 (oxy)hydroxides mean reduced Co^{3+} to Co^{4+} oxidation. Both agree with our DFT predictions.

We further employed Quasi-operando EELS to investigate the Co valence changes during OER. EELS spectra of Co, Fe, and Cr were collected after biasing catalysts loaded on an Au TEM grid under open-circuit potential (V_{OC}), 1.4, and 1.5 V_{RHE} for 10 min in a 0.5 M $KHCO_3$ electrolyte. Their normalized Co L-edge spectra are displayed in **Figure 5**a and Figure S24, Supporting Information. The Co-L_3 and L_2 edges in all catalysts gradually shift to higher loss energies with increased anodic potentials, suggesting the formation of high valence Co species. The Co-L_3/L_2 edge intensity ratios are calculated and tabulated in Table S7, Supporting Information for quantitative comparison. As shown in Figure 5b, the Co-L_3/L_2 area ratio of $Co_5Fe_3Cr_2$ exhibits the fastest decline among the four catalysts. It quickly decreases from 3.64 at V_{OC} to 2.99 at 1.4 V_{RHE}, which is lower than Co_3O_4 at 3.28 (Figure S25, Supporting Information). It further drops to 2.69 at 1.5 V_{RHE}, which is lower than a reference CoOOH at 2.74 (Figure S10, Supporting Information), indicating the transformation of Co species to catalytic active $Co^{3+\delta}$ ($0 < \delta < 1$).[4b] In comparison, higher Co L_3/L_2 ratios in Co_5Fe_5, Co_5Cr_5, and Co (oxy)hydroxides suggest higher Co^{2+} remnants, which is indicative of their slower $Co^{3+\delta}$ formation. The quasi-operando EELS results support our DFT results that the incorporation of Fe and Cr accelerates the formation of high valence Co species. The accelerated formation of high-valence Co active sites would also improve catalysts' performance in neutral electrolytes.[13] As shown in Figure 5c, $Co_5Fe_3Cr_2$ requires an η_{10} of 452 mV in a 0.5 M $KHCO_3$ electrolyte, outperforming IrO_2 at 497 mV and other catalysts prepared in this study.

We also measured the quasi-operando EELS spectra of Fe and Cr. The Fe-L_3 and Cr-L_3 edge shifts by 0.3 and 2.2 eV toward higher loss energies, indicating their increased valence states (Figure S26, Supporting Information). The fitting of the Cr EELS spectrum obtained at 1.5 V using simulated Cr^{x+} features

further confirms the formation of abundant high valence Cr^{5+} and Cr^{6+} species (Figure S27, Supporting Information), agreeing with the post-stability test XPS results displayed in Figure S22, Supporting Information. While XPS measurement exhibits shallow penetration depth that prohibits the examination of bulk catalyst properties, the EELS spectra collected from TEM can lift this limitation. The good agreement between our XPS and EELS measurement further confirmed the bulk structure transformation and valence increment of the metal elements in this trimetallic CoFeCr oxyhydroxide OER electrocatalyst.

3. Conclusion

In summary, we show that Cr plays a critical role in enabling ternary Co–Fe–Cr (oxy)hydroxide as an excellent OER catalyst in both alkaline and neutral electrolytes. Initial DFT simulation results suggest that Cr may promote Co's valence state transition under OER condition and improve Co's activity via electronic synergies. Experimental X-ray spectroscopic results confirm that Cr promotes Co's occupation in octahedral sites and modulates Co's electronic structures. At the optimal composition, $Co_5Fe_3Cr_2$ (oxy)hydroxides catalyst deliver a low η_{10} of 232 mV, a high Co-based mass activity of 1486.0 A g^{-1}, and a superior TOF of 0.23 s^{-1}. Quasi-operando EELS studies validate the initial DFT prediction that Cr accelerates the deprotonation-coupled pre-oxidation of Co^{2+} to Co^{3+} or $Co^{3+\delta}$, leading to significantly improved catalytic activity. Understanding the role of Cr and the determined optimal elemental composition of Co–Fe–Cr (oxy)hydroxides opens the door for their practical energy storage and conversion applications as an efficient OER catalyst.

4. Experimental Section

Computational Methods: DFT calculations were performed using the VASP code with spin-polarization and Hubbard-U corrections (DFT + U). Electron correlation was applied using a generalized gradient approximation method and the RPBE functional,[24] while the core electrons were applied with a projector augmented-wave method.[25] The valence electrons were expanded as Kohn–Sham wave functions in a plane-wave basis set.[26] The Brillouin zone for the bulk and surface models were respectively sampled using ($10 \times 10 \times 10$) and ($3 \times 3 \times 1$) Monkhorst–Pack k-point meshes and integrated with the Methfessel and Paxton method.[27] A vacuum gap of at least 15 Å was applied in
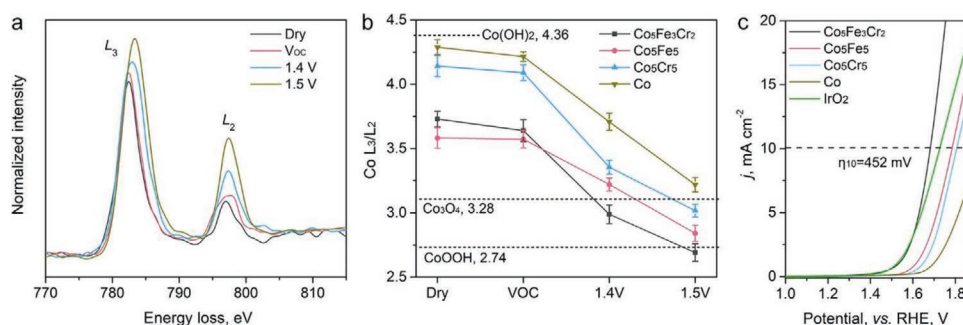

Figure 5. Probing Co valence transitions. a) Quasi-operando Co L-edge EELS spectra of $Co_5Fe_3Cr_2$ after being biased at different potentials and b) calculated Co L_3/L_2 ratios of catalysts under different potentials. c) OER LSV curves of various catalysts in 0.5 M $KHCO_3$ neutral electrolyte.

the z-direction of each surface model. The use of U_{eff} (U − J) values for the cation elements was based on the Materials Project database (https://materialsproject.org/). Geometries of the bulk and surface models were defined as converged when all the atom forces fell below 0.05 and 0.01 eV Å^{-1}, respectively. A dipole moment correction was applied to correct the residual dipole moments perpendicular to the surface model. The OER volcano activity plot was developed using the method derived by Bajdich et al.[6a] The formation energies of bulk models were calculated using H_2 molecules in the gas phase as the energy reference. The CoOOH model was comprised of four layers of 2 × 3 (10$\bar{1}$4) surfaces due to its proven higher thermodynamic OER activity and stability.[6a] For the bulk systems, the binary CoFeOOH and CoCrOOH models were developed by replacing half of the Co atoms in CoOOH with Fe or Cr. The ternary CoFeCrOOH model was developed by replacing half of the Co atoms in CoOOH by both Fe and Cr at a 1:1 ratio. For the surface models, the bottom two layers were held fixed in bulk positions, while the topmost two layers were allowed to relax. The computational hydrogen electrode (CHE) method was used to calculate the OER free energies in Figure 4g.[28] The calculated theoretical overpotentials in Figure 4h are independent of pH or potential values,[22] since the free energies shifted in the same way with different potential or pH, and lead to the same potential-limiting step. Previous studies also had shown that this CHE-based free energy calculation method resulted in excellent agreement with the experimental OER overpotentials for a large number of transition metal oxides under both alkaline and acidic conditions. Zero-point energy corrections were applied to all the free energy calculations using reference data.[6a] The entropic corrections were applied to the gas-phase molecules with a temperature of 298.15 K.

Material Synthesis: $CoCl_2 \cdot 6H_2O$, $FeCl_3 \cdot 6H_2O$, and $KCr(SO_4)_2 \cdot 12H_2O$ were obtained from Sigma Aldrich and used as received to prepare salt stock solutions at a concentration of 0.2 м. An appropriate amount of salt solutions were mixed and diluted with DI water to 10 mL, and the total metal anion concentration was kept at 20 mм. The metal precursor solution was then injected by a peristaltic pump into 50 mL of hot 0.2 м urea solution at 90 °C in 20 min under vigorous stirring. The mixture solution was further kept stirring at 90 °C for an additional 6 h before the metal (oxy)hydroxide precipitates were collected by centrifugation, washed with DI water and ethanol, and finally dried at 60 °C in an oven overnight. IrO_2 catalyst (Fuelcell Store) was used as a reference catalyst.

Material Characterization: Elemental composition was confirmed by ICP-AES on a Varian Vista Pro instrument. SEM observation was performed on a Zeiss Ultra Plus SEM. (S)TEM, SAED, and EDX mapping were tested on an FEI Themis-Z microscope. XRD patterns were obtained on a Shimadzu XRD-6000 diffractometer. XAS of various catalysts were collected at Beamline 1W1B at Beijing Synchrotron Radiation Facility. Standard Fe_2O_3, Cr_2O_3, and CoOOH were used as references. All spectra were processed and analyzed in the Demeter software package using the FEFF code. XPS spectra were collected on a K-Alpha+ (Thermo Fisher Scientific) spectrometer equipped with an Al-Kα (1486.3 eV) source. All energy was corrected with a standard graphite sample. EELS spectra were collected on a Joel-2200FS microscope at 80 keV with a collection angle of 40 mrad. The quasi-operando EELS measurement was performed by loading the catalysts on an Au TEM grid. The TEM grids were mounted on a screen-printed carbon electrode (RRPE1002C, Pine Research) with an integrated Ag/AgCl reference electrode and graphite counter electrode. About 2 mL of 0.5 м neutral $KHCO_3$ electrolyte (pH = 7.8) was put on top of the electrode, and the catalyst was biased at various potentials for 10 min before the TEM grid was quickly dismounted, blow-dried with dry N_2, and rapidly quenched with liquid N_2. The spectra were collected with a comparable electron dosage (5 × 10^6 electrons Å^{-2}) for each measurement.

Electrochemical Measurement: Electrocatalyst ink was prepared by dispersing catalysts in a 1/9 water/isopropanol v/v solution at 1 mg mL^{-1} with 0.05% wt v^{-1} Nafion 117 (Sigma). The ink was drop-cast on a rotary GCE (Pine instrument, $\varnothing$ = 5 mm) at an areal mass loading at 0.2 mg cm^{-2}. The electrochemical performance was tested on an electrochemical

workstation (CHI 760E) in the three-electrode configuration with a Pt mesh as a counter electrode, and a Hg/HgO reference electrode (1 м KOH filling) as a reference electrode in O_2 saturated 1 м KOH or 0.5 м $KHCO_3$ electrolyte. All potentials reported were corrected to the reversible hydrogen electrode (RHE) by adding 0.140 + 0.059 × pH. The stability test was performed in 1 м KOH electrolyte. For stability tests, the catalyst was loaded on a Ni foam electrode with a mass loading of 0.2 mg cm^{-2}. A $MoNi_4$ on Ni foam electrode ($MoNi_4$/NF) was prepared following a reported method[21] and used as the counter electrode.

CV curves were obtained at a scan rate of 50 mV s^{-1}. LSV polarization and Tafel plots were obtained at a rate 5 mV s^{-1} without *iR* correction. EIS tests were performed at η = 300 mV. ECSA of the catalysts was determined by CV scans performed in a non-Faradaic region in 1 м KOH electrolyte. The cathodic and anodic currents at the mid-point were linear fit, and the absolute slopes were averaged and taken as the C_{dl} of the catalyst. C_s of 0.04 mF cm^{-2}[2f] was used to estimate the ECSA for various electrocatalysts using ECSA = C_{dl}/C_s (cm^2). The TOF of various catalysts was calculated using Equation (5):

$$TOF = \frac{i \times FE}{4 \times F \times n} \tag{5}$$

where *i* (A) is the current obtained at η = 300 (with 95% *iR*-correction), *FE* is the Faradaic efficiency determined by the RRDE method. *F* is the Faraday constant (96485 C mol^{-1}), and *n* is the mole number of catalysts on the electrode.

The carrier density (C_d) in the catalysts was determined from EIS measurements performed at different applied potentials from 0 to 0.5 V (vs SCE) following a reported method.[29] The capacitance calculated at 0.1 Hz was plotted against the potential to develop the Mott–Schottky plot. The fitted slope of the linear part was used to calculate C_d using Equation (6):

$$\frac{1}{C_d^2} = \frac{2}{e \varepsilon \varepsilon_0 N_A} \left(V - V_f - \frac{kT}{e} \right) \tag{6}$$

where *e* is the charge of an electron (1.602 × 10^{-19} C), ε_0 is free space permittivity (8.85 × 10^{-14} F cm^{-1}), and ε is the dielectric constant of oxides, an estimated value of 20 was used.

Supporting Information

Supporting Information is available from the Wiley Online Library or from the author.

Acknowledgements

Conflict of Interest

The authors declare no conflict of interest.

Data Availability Statement

Data available on request from the authors.

Keywords

[1] a) N.-T. Suen, S.-F. Hung, Q. Quan, N. Zhang, Y.-J. Xu, H. M. Chen, *Chem. Soc. Rev.* **2017**, *46*, 337; b) M. Tahir, L. Pan, F. Idrees, X. Zhang, L. Wang, J.-J. Zou, Z. L. Wang, *Nano Energy* **2017**, *37*, 136.

[2] a) S. Anantharaj, K. Karthick, S. Kundu, *Mater. Today Energy* **2017**, *6*, 1; b) J. R. Galán-Mascarós, *ChemElectroChem* **2015**, *2*, 37; c) I. Roger, M. A. Shipman, M. D. Symes, *Nat. Rev. Chem.* **2017**, *1*, 0003; d) M. Gong, D.-Y. Wang, C.-C. Chen, B.-J. Hwang, H. Dai, *Nano Res.* **2016**, *9*, 28; e) M. S. Burke, L. J. Enman, A. S. Batchellor, S. Zou, S. W. Boettcher, *Chem. Mater.* **2015**, *27*, 7549; f) C. C. L. McCrory, S. Jung, J. C. Peters, T. F. Jaramillo, *J. Am. Chem. Soc.* **2013**, *135*, 16977.

[3] J. Suntivich, K. J. May, H. A. Gasteiger, J. B. Goodenough, Y. Shao-Horn, *Science* **2011**, *334*, 1383.

[4] a) Y. Surendranath, M. W. Kanan, D. G. Nocera, *J. Am. Chem. Soc.* **2010**, *132*, 16501; b) A. Bergmann, T. E. Jones, E. M. Moreno, D. Teschner, P. Chernev, M. Gliech, T. Reier, H. Dau, P. Strasser, *Nat. Catal.* **2018**, *1*, 711; c) J. Zhou, Y. Wang, X. Su, S. Gu, R. Liu, Y. Huang, S. Yan, J. Li, S. Zhang, *Energy Environ. Sci.* **2019**, *12*, 739; d) B. Zhang, X. Zheng, O. Voznyy, R. Comin, M. Bajdich, M. García-Melchor, L. Han, J. Xu, M. Liu, L. Zheng, F. P. García de Arquer, C. T. Dinh, F. Fan, M. Yuan, E. Yassitepe, N. Chen, T. Regier, P. Liu, Y. Li, P. De Luna, A. Janmohamed, H. L. Xin, H. Yang, A. Vojvodic, E. H. Sargent, *Science* **2016**, *352*, 333; e) J. Chen, H. Li, Z. Yu, C. Liu, Z. Yuan, C. Wang, S. Zhao, G. Henkelman, S. Li, L. Wei, Y. Chen, *Adv. Energy Mater.* **2020**, *10*, 2002593.

[5] a) S. Hao, L. Chen, C. Yu, B. Yang, Z. Li, Y. Hou, L. Lei, X. Zhang, *ACS Energy Lett.* **2019**, *4*, 952; b) F. Qin, Z. Zhao, M. K. Alam, Y. Ni, F. Robles-Hernandez, L. Yu, S. Chen, Z. Ren, Z. Wang, J. Bao, *ACS Energy Lett.* **2018**, *3*, 546.

[6] a) M. Bajdich, M. García-Mota, A. Vojvodic, J. K. Nørskov, A. T. Bell, *J. Am. Chem. Soc.* **2013**, *135*, 13521; b) M. T. Koper, *J. Electroanal. Chem.* **2011**, *660*, 254; c) Z. W. Seh, J. Kibsgaard, C. F. Dickens, I. Chorkendorff, J. K. Nørskov, T. F. Jaramillo, *Science* **2017**, *355*, eaad4998.

[7] a) L. Xu, Q. Jiang, Z. Xiao, X. Li, J. Huo, S. Wang, L. Dai, *Angew. Chem., Int. Ed.* **2016**, *55*, 5277; b) R. Zhang, Y.-C. Zhang, L. Pan, G.-Q. Shen, N. Mahmood, Y.-H. Ma, Y. Shi, W. Jia, L. Wang, X. Zhang, W. Xu, J.-J. Zou, *ACS Catal.* **2018**, *8*, 3803.

[8] a) J. Masa, P. Weide, D. Peeters, I. Sinev, W. Xia, Z. Sun, C. Somsen, M. Muhler, W. Schuhmann, *Adv. Energy Mater.* **2016**, *6*, 201600980; b) S. Chen, J. Duan, P. Bian, Y. Tang, R. Zheng, S.-Z. Qiao, *Adv. Energy Mater.* **2015**, *5*, 1500936; c) Z. Wang, H. Liu, R. Ge, X. Ren, J. Ren, D. Yang, L. Zhang, X. Sun, *ACS Catal.* **2018**, *8*, 2236; d) M. Chauhan, K. P. Reddy, C. S. Gopinath, S. Deka, *ACS Catal.* **2017**, *7*, 5871.

[9] a) W. Liu, H. Liu, L. Dang, H. Zhang, X. Wu, B. Yang, Z. Li, X. Zhang, L. Lei, S. Jin, *Adv. Funct. Mater.* **2017**, *27*, 1603904; b) M. S. Burke, M. G. Kast, L. Trotochaud, A. M. Smith, S. W. Boettcher, *J. Am. Chem. Soc.* **2015**, *137*, 3638; c) F. Song, X. Hu, *J. Am. Chem. Soc.* **2014**, *136*, 16481; d) H. Liang, F. Meng, M. Cabán-Acevedo, L. Li, A. Forticaux, L. Xiu, Z. Wang, S. Jin, *Nano Lett.* **2015**, *15*, 1421.

[10] a) C. Dong, X. Yuan, X. Wang, X. Liu, W. Dong, R. Wang, Y. Duan, F. Huang, *J. Mater. Chem. A* **2016**, *4*, 11292; b) X. Bo, Y. Li, X. Chen, C. Zhao, *J. Power Sources* **2018**, *402*, 381; c) C.-C. Lin, C. C. L. McCrory, *ACS Catal.* **2017**, *7*, 443; d) Y. Yang, L. Dang, M. J. Shearer, H. Sheng, W. Li, J. Chen, P. Xiao, Y. Zhang, R. J. Hamers, S. Jin, *Adv. Energy Mater.* **2018**, *8*, 1703189; e) X. Bo, Y. Li, R. K. Hocking, C. Zhao, *ACS Appl. Mater. Interfaces* **2017**, *9*, 41239; f) X. Bo, Y. Li, X. Chen, C. Zhao, *Chem. Mater.* **2020**, *32*, 4303; g) L. Fan, P. Zhang, B. Zhang, Q. Daniel, B. J. J. Timmer, F. Zhang, L. Sun, *ACS Energy Lett.* **2018**, *3*, 2865.

[11] J. B. Gerken, J. G. McAlpin, J. Y. C. Chen, M. L. Rigsby, W. H. Casey, R. D. Britt, S. S. Stahl, *J. Am. Chem. Soc.* **2011**, *133*, 14431.

[12] a) J. Chen, H. Li, Z. Pei, Q. Huang, Z. Yuan, C. Wang, X. Liao, G. Henkelman, Y. Chen, L. Wei, *J. Mater. Chem. A* **2020**, *8*, 15951; b) C. Lee, K. Shin, C. Jung, P.-P. Choi, G. Henkelman, H. M. Lee, *ACS Catal.* **2020**, *10*, 562.

[13] X. Zheng, B. Zhang, P. De Luna, Y. Liang, R. Comin, O. Voznyy, L. Han, F. P. García de Arquer, M. Liu, C. T. Dinh, T. Regier, J. J. Dynes, S. He, H. L. Xin, H. Peng, D. Prendergast, X. Du, E. H. Sargent, *Nat. Chem.* **2017**, *10*, 149.

[14] H.-Y. Wang, S.-F. Hung, H.-Y. Chen, T.-S. Chan, H. M. Chen, B. Liu, *J. Am. Chem. Soc.* **2016**, *138*, 36.

[15] R. L. Burwell, G. L. Haller, K. C. Taylor, J. F. Read, in *Advances in Catalysis*, Vol. *20*, (Eds: D. D. Eley, H. Pines, P. B. Weisz), Academic Press, Cambridge **1969**.

[16] a) J. Gázquez, G. Sánchez-Santolino, N. Biškup, M. A. Roldán, M. Cabero, S. J. Pennycook, M. Varela, *Mater. Sci. Semicond. Process.* **2017**, *65*, 49; b) D. H. Pearson, C. C. Ahn, B. Fultz, *Phys. Rev. B* **1993**, *47*, 8471.

[17] H. Tan, J. Verbeeck, A. Abakumov, G. Van Tendeloo, *Ultramicroscopy* **2012**, *116*, 24.

[18] C. Mu, J. Mao, J. Guo, Q. Guo, Z. Li, W. Qin, Z. Hu, K. Davey, T. Ling, S.-Z. Qiao, *Adv. Mater.* **2020**, *32*, 1907168.

[19] a) J. Suntivich, W. T. Hong, Y.-L. Lee, J. M. Rondinelli, W. Yang, J. B. Goodenough, B. Dabrowski, J. W. Freeland, Y. Shao-Horn, *J. Phys. Chem. C* **2014**, *118*, 1856; b) F. M. F. de Groot, M. Grioni, J. C. Fuggle, J. Ghijsen, G. A. Sawatzky, H. Petersen, *Phys. Rev. B* **1989**, *40*, 5715.

[20] a) S. Yagi, I. Yamada, H. Tsukasaki, A. Seno, M. Murakami, H. Fujii, H. Chen, N. Umezawa, H. Abe, N. Nishiyama, S. Mori, *Nat. Commun.* **2015**, *6*, 8249; b) W. T. Hong, R. E. Welsch, Y. Shao-Horn, *J. Phys. Chem. C* **2016**, *120*, 78.

[21] J. Zhang, T. Wang, P. Liu, Z. Liao, S. Liu, X. Zhuang, M. Chen, E. Zschech, X. Feng, *Nat. Commun.* **2017**, *8*, 15437.

[22] I. C. Man, H.-Y. Su, F. Calle-Vallejo, H. A. Hansen, J. I. Martínez, N. G. Inoglu, J. Kitchin, T. F. Jaramillo, J. K. Nørskov, J. Rossmeisl, *ChemCatChem* **2011**, *3*, 1159.

[23] R. D. L. Smith, C. Pasquini, S. Loos, P. Chernev, K. Klingan, P. Kubella, M. R. Mohammadi, D. Gonzalez-Flores, H. Dau, *Nat. Commun.* **2017**, *8*, 2022.

[24] a) J. P. Perdew, K. Burke, M. Ernzerhof, *Phys. Rev. Lett.* **1996**, *77*, 3865; b) B. Hammer, L. B. Hansen, J. K. Nørskov, *Phys. Rev. B* **1999**, *59*, 7413.

[25] P. E. Blöchl, *Phys. Rev. B* **1994**, *50*, 17953.

[26] W. Kohn, L. J. Sham, *Phys. Rev.* **1965**, *140*, A1133.

[27] H. J. Monkhorst, J. D. Pack, *Phys. Rev. B* **1976**, *13*, 5188.

[28] J. K. Nørskov, J. Rossmeisl, A. Logadottir, L. Lindqvist, J. R. Kitchin, T. Bligaard, H. Jónsson, *J. Phys. Chem. B* **2004**, *108*, 17886.

[29] T. W. Kim, K.-S. Choi, *Science* **2014**, *343*, 990.